SANDIA REPORT
SAND98–1210
Unlimited Release
Printed June 1998

Understanding and Control of Optical Performance from Ceramic Materials

J. C. Barbour, B. G. Potter, D. R. Jennison, C. A. Verdozzi, J. A. Knapp, D. M. Follstaedt, R. D. Bendale, J. H. Simmons

Prepared by
Sandia National Laboratories
Albuquerque, New Mexico 87185 and Livermore, California 94550

Sandia is a multiprogram laboratory operated by Sandia Corporation, a Lockheed Martin Company, for the United States Department of Energy under Contract DE-AC04-94AL85000.

Sandia National Laboratories

Issued by Sandia National Laboratories, operated for the United States Department of Energy by Sandia Corporation.

Available to DOE and DOE contractors from
Office of Scientific and Technical Information
P.O. Box 62
Oak Ridge, TN 37831

Prices available from (615) 576-8401, FTS 626-8401

Available to the public from
National Technical Information Service
U.S. Department of Commerce
5285 Port Royal Rd
Springfield, VA 22161

NTIS price codes
Printed copy: A03
Microfiche copy: A01

SAND98-1210
Unlimited Release
Dated June 1998

Understanding and Control of Optical Performance From Ceramic Materials

J. C. Barbour and J. A. Knapp
Radiation Solid Interactions and Processing Department
B. G. Potter
Electronic and Optical Materials Department
D. R. Jennison and C. A. Verdozzi
Surface and Interface Science Department
D. M. Follstaedt
Nanostructure and Semiconductor Physics Department
Sandia National Laboratories
Albuquerque, NM 87185-1056

R. D. Bendale and J. H. Simmons
Materials Science and Engineering Department
University of Florida
Gainesville, FL 32611

Abstract

This report summarizes a two-year Laboratory-Directed Research and Development (LDRD) program to gain understanding and control of the important parameters which govern the optical performance of rare-earth (RE) doped ceramics. This LDRD developed the capability to determine stable atomic arrangements in RE doped alumina using local density functional theory, and to model the luminescence from RE-doped alumina using molecular dynamic simulations combined with crystal-field calculations. Local structural features for different phases of alumina were examined experimentally by comparing their photoluminescence spectra and the atomic arrangement of the amorphous phase was determined to be similar to that of the gamma phase. The luminescence lifetimes were correlated to these differences in the local structure. The design of both high and low-phonon energy host materials was demonstrated through the growth of Er-doped aluminum oxide and lanthanum oxide. Multicomponent structures of rare-earth doped telluride glass in an alumina and silica matrix were also prepared. Finally, the optical performance of Er-doped alumina was determined as a function of hydrogen content in the host matrix. This LDRD is the groundwork for future experimentation to understand the effects of ionizing radiation on the optical properties of RE-doped ceramic materials used in space and other radiation environments.

Key Words: optical ceramic materials, luminescence, rare-earth doped, molecular dynamic simulation, ab-initio calculations

Acknowledgments

Carl Seager and Mike Sinclair collaborated on this project by measuring the optical properties of Er-doped alumina, and Peter Schultz and Mark Sears modified the QUEST computer code to enable calculations of aluminum oxide and La-doped aluminum oxide structures. The technical assistance of Ken Minor was invaluable for the growth and ion implantation needed in these studies. The technical assistance of Mike Moran was invaluable for the TEM sample preparation and analysis, and the technical assistance of Dan Buller was invaluable for ion beam analysis and for ion-stimulated luminescence measurements.

This work was supported by the U.S. Department of Energy under contract DE-AC04-94AL85000.

Contents

This Page Intentionally Left Blank

Understanding and Control of Optical Performance from Ceramic Materials

I. Introduction

Materials containing trivalent rare-earth (RE) ions are critical to the operation of a range of optical devices based on the emissive properties of the dopant, e.g. optical amplifiers/lasers and solid-state light sources for integrated photonics. Synthesis of a suitable RE host is extremely important as the optical performance of the dopant is largely determined by the local environment provided by the host. Currently, emissive sources and gain media for optical communications are designed around the low dispersion (1.3 μm) or low loss (1.54 μm) wavelengths for SiO_2 optical fibers. For both of these wavelengths, light emission relies on the excited-state behavior of rare-earth (RE) ions incorporated in a homogeneous host material. However, future defense and industrial applications will require higher communication rates and greater data storage densities than those achievable with current optical components. Therefore, the creation of broad-band, lossless optical components with an increased operational wavelength range is of critical importance to these technologies, and will depend upon the development of new RE-ion hosts that can insure optimum optical performance and continued physical compatibility with operational requirements. While single-phase materials require compromises to be made between these two requirements, a multiphase host furnishes the structural versatility to simultaneously satisfy both conditions. Efficient and accurate design and construction of such hosts, however, requires a fundamental understanding of how nanoscale heterogeneities will mediate radiative and nonradiative energy transfer mechanisms and the local structural environments of the RE ions. The development of a predictive modeling capability based on this understanding would enable new materials systems and concepts for composite materials to be evaluated on the computer prior to fabrication. This LDRD focused on the development of modeling and experimental capabilities to understand how to improve the optical performance of rare-earth doped ceramics such as alumina. Stable atomic arrangements in RE doped phases were determined using ab-initio calculations, and the luminescence from RE-doped phases was modeled using molecular dynamic simulations combined with crystal-field calculations.

II. The Growth of Er-Doped Amorphous and Crystalline Al_2O_3 And La_2O_3.

The experimental portion of this LDRD developed the capability to manufacture rare-earth doped oxide films through ion implantation, plasma deposition, and pulsed-laser deposition (PLD). These films were needed in order to supply the experimental verification for the modeling effort. Representative sample geometries envisioned in the original proposal are shown schematically in Fig. 1 in which the local environment of the RE ion could be modified by phase and composition to effect a modification of the luminescence properties. Our ability to make these types of samples and to effect changes in the luminescence properties will be demonstrated in the next two subsections.

A. Phase Control

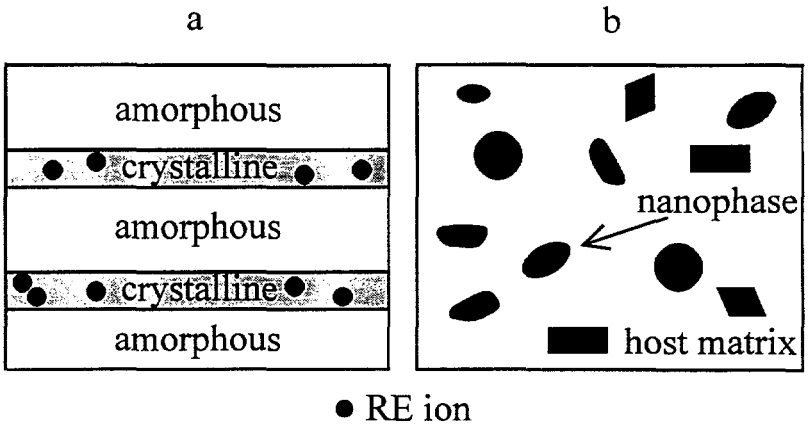

Fig. 1. Representations for possible composite structures.

The optical performance of Er-doped oxides can be modified through atomic-level engineering of the Er local atomic structural environment in different optical-ceramic host materials. To this end, this work experimentally manipulated the local environment of erbium ions in different phases of Al_2O_3 and La_2O_3 in order to understand the impact of the host-ion interaction on luminescence efficiency and lifetimes, τ (both crystal field and phonon effects were considered). These experimental results can be used to evaluate and modify theoretical models of these optical ceramic systems in order to predict, *a priori*, the optical behavior of Er^{+3} in different host materials (see section III B). Low temperature deposition of this important class of materials is needed for integrated optical amplifier components on III-V semiconductors, and therefore the formation of these different phases at low temperature was studied using an electron cyclotron resonance (ECR) plasma.

Previously [1], we showed that ECR O_2 plasmas combined with electron beam evaporation can form Al_2O_3 in either the amorphous (a-Al_2O_3) or the fcc γ-phase by varying the ion energy and temperature during deposition. An ECR-Al_2O_3 layer deposited at $\leq$ 400°C without a bias is amorphous, while an ECR-Al_2O_3 layer deposited at 400°C with a bias $\geq$ 140 V is polycrystalline γ-Al_2O_3. The γ phase has the spinel structure which is an fcc lattice with O occupying the fcc lattice sites and Al occupying octahedral (o) and tetrahedral (t) sites within the O lattice. This phase has a lattice constant a=0.7859 nm [2] and an atomic density of 1.10×10^{23} at/cm^3. The Al can occupy these o and t sites in an ordered fashion under some circumstances, but for ECR-deposited films, we believe the Al is occupying the many o and t sites, randomly. The lattice location for Er in the γ phase has not been measured, but theoretical calculations [3] indicate that it should occupy a site displaced slightly from the o interstitial position. For comparison, the lattice-site location of Er in sapphire (α-Al_2O_3) has been measured [4], and 70% of the Er is incorporated near the free o site (0.08 nm displaced along the c-axis) and 20% is incorporated in a t site. Ab-initio calculations based on local density functional theory [5] (see section III A) have confirmed that this slight displacement away from the o site is the lowest energy configuration for a lanthanide ion in α-Al_2O_3. Sapphire is a hexagonal phase with nearly the same atomic density (1.18×10^{23} at/cm^3) as the γ phase. Again, oxygen occupies the close-packed lattice sites of the hexagonal phase, and Al occupies o interstitial sites in an ordered fashion within the oxygen lattice. The lattice constants for α-Al_2O_3 are: a=0.4754 nm and c=1.299 nm [2]. The local atomic environment for Er in a-Al_2O_3 has not been measured or calculated theoretically.

Based on the similarity between the expected local configuration for Er in the α and γ phases, the photoluminescence (PL) spectra for Er in these phases should be similar but possibly different from that for Er in a-Al_2O_3. This subsection compares PL spectra from these different phases, and then examines PL from another hexagonal phase, La_2O_3, with a higher mass metal element which yields lower phonon energies.

Erbium-doped aluminum and lanthanum oxide layers were deposited onto Si and oxidized Si substrates using an electron-beam evaporation source downstream from a horizontally positioned ECR plasma source. The ECR plasma allows for operation in the low pressure regimes needed for the metal deposition. Microwaves (80-130 Watts) at a frequency of 2.45 GHz were injected into the ECR chamber to excite the O_2 gas, forming neutral atoms and molecular ions. The highly reactive oxygen species stream down from this plasma generation region onto the layer and substrate. The ECR system base pressure was $\approx 0.3 \times 10^{-8}$ Torr, and the operating pressure was $3\text{-}5 \times 10^{-5}$ Torr with an O_2 gas flow rate of 2.5 sccm. Evaporation rates for Al (or La) and Er were measured simultaneously using two quartz crystal monitors, and films were grown at 0.2 nm/s for Al (La) while simultaneously evaporating Er at 0.01-0.03 nm/s.

The composition, phase, and optical properties of ECR-grown films were measured as a function of ion energy and growth temperature from 35°C to 400°C. Samples were either electrically isolated relative to ground (the chamber walls) during growth, yielding a minimum ion energy ($\approx$30 eV) incident from the plasma onto the substrate, or the sample was biased at -100 to -300 V yielding ion energies of 130 to 330 eV during deposition. For comparison to the ECR-deposited amorphous and γ-phases, an Er-ion implanted sapphire sample was prepared for photoluminescence spectral analysis. The single-crystal sapphire wafer was sequentially implanted at room temperature and vacuum annealed at 900°C to form a $\approx$250 nm thick layer with 0.2 at.% Er. The following Er ion fluences and energies were used to obtain a nearly constant composition: 3.2×10^{14} cm^{-2} at 100 keV, 4.4×10^{14} cm^{-2} at 190 keV, 8.0×10^{14} cm^{-2} at 330 keV, and 1.6×10^{15} cm^{-2} at 660 keV. The composition of all samples were obtained by using 2.8 MeV He^+ Rutherford Backscattering spectrometry (RBS) at a scattering angle of 164°, and by using 22-24 MeV Si^{+5} Elastic Recoil Detection (ERD) at a scattering angle of 30°. Both planar (TEM) and cross-sectional (XTEM) transmission electron microscopy were done to evaluate the microstructure and phase of the ECR-deposited materials. The planar TEM was obtained from thin films deposited on SiO_n-coated TEM grids.

Laser excited photoluminescence (PL) spectra were collected from samples at both room temperature (RT) and 15-16 K to examine phonon-mediated effects on the spectral and temporal behavior of the 1.54 μm emission from Er^{+3} within the different host materials (a-Al_2O_3, γ-Al_2O_3, α-Al_2O_3, and La_2O_3). An Ar-ion laser was used to excite the samples with 488 nm light. The PL spectra were collected using a closed-loop, cryogenic cooler with optical access. This equipment allows two samples to be mounted and cooled simultaneously. Emission was collected in a reflection geometry and the spectral analysis was performed using a 0.275 m monochromator equipped with a liquid-nitrogen cooled Ge detector. The RT data were collected with the samples mounted in the cryogenic chamber under vacuum, for comparing to the cryogenic spectra. There was no movement of samples between the measurements, allowing relative changes in emission intensity to be examined. Luminescence intensity comparisons between samples were also possible, given the invariance of the excitation geometry and excitation powers.

As stated above, the use of a biased plasma and temperatures ≥ 400°C during growth varies the phase formation from a-Al_2O_3 at lower temperatures, without a bias, to γ-Al_2O_3 at higher temperatures, with a bias. Moreover, the use of a bias at lower temperatures can also vary the density of the sample while keeping the amorphous phase. The index of refraction, n, as determined from reflectometry measurements (not shown) of samples grown at 150-160°C, was found to increase from n=1.637 for a sample deposited at the floating potential with 30 eV ions to n=1.647 for a sample deposited with a bias of -125 V (155 eV O_2^+ ions). This increase in n is representative of an increase in the sample density for low energy ion-assisted growth. Further, the sample grown without a bias has a higher hydrogen content, 0.5-2.0 at.%, than the sample grown with a bias of -125 V, 0.1-0.8 at.%. This decrease in H content with increasing bias is consistent with a more dense amorphous structure containing fewer dangling bonds for attachment of the H. In a separate experiment, hydrogen was shown to be incorporated during deposition from residual H attached to the chamber walls.

In order to demonstrate the ability to form a structured sample as depicted in Fig. 1 a, multilayer samples were grown with alternating amorphous and γ-phase layers, without breaking vacuum. The samples that were grown had sharp interfaces between the amorphous and crystalline phases and appeared rather remarkably like the schematic image first envisioned (as shown in fig. 1). Fig. 2. Shows a bright-field cross-section transmission electron microscope (XTEM) image taken from one of these multilayered samples at -1.2 μm underfocus to enhance the Fresnel contrast, demonstrating the lower electron density in the lighter colored layer. The crystalline layers were the first and last layers grown and have a low hydrogen content. The amorphous layer had a higher hydrogen content than the γ phase even though it was heated to 400°C for the γ-phase growth. This interdigitated high-density/low-density Al_2O_3 sample was prepared at high temperature on Si by successively changing the bias from -200 V to 0 V while simultaneously ramping the temperature between ≈400°C and 130°C. The light layer at the bottom of the figure is crystalline Si and the next layer above was grown with a bias and forms γ-Al_2O_3 with a high-density, large-grain columnar structure. The layer above is amorphous Al_2O_3 with no visible grain structure, and then the top layer is γ-Al_2O_3 again grown with a bias. This sample demonstrates that the growth of the crystalline or amorphous layers is dependent upon the growth conditions rather than the crystallinity of the layer on which it is growing. In other words, the crystalline phase did not act as a template to continue growth of the crystalline phase even though the growth conditions favored an amorphous phase. Also, the crystalline phase can be made to grow on an amorphous phase without altering the structure of the amorphous phase.

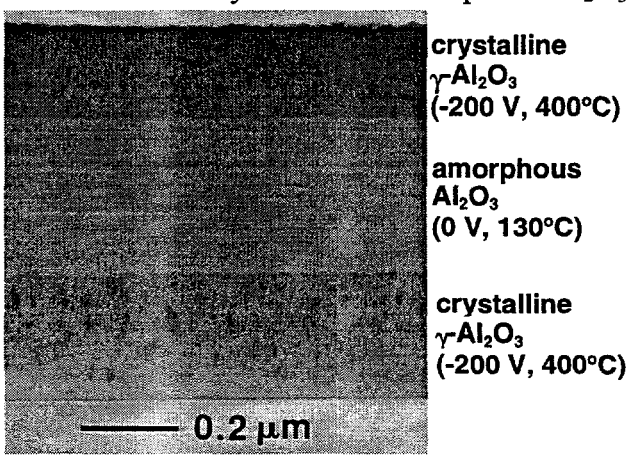

Fig. 2. Bright-field XTEM micrograph demonstrating the growth of the composite structure given in Fig. 1a. These interdigitated amorphous and γ Al_2O_3 layers were deposited with the conditions shown.

PL spectra collected at 300 K, depicting the $^4I_{13/2}$ to $^4I_{15/2}$ radiative transition for Er^{+3} in Al_2O_3 are shown in Fig 3. For comparison, the PL spectrum from an Er-

implanted, fused silica sample is also shown in this figure (bottom curve). The curves were offset along the vertical axis for clarity, and the relative intensities should not be compared. However, the peak positions for these samples can be compared. The upper curve (dashed line) is from an as-grown 1100 nm thick, 0.2 at.% Er-doped γ layer grown on an oxidized Si wafer at 400°C with a bias of -200 V (τ=5.7 ms). The solid line is the spectrum from a ≈ 250 nm thick, 0.2 at.% Er-implanted α-Al_2O_3 which was annealed to 900°C in order to eliminate the implantation damage (τ=2.3 ms). The spectrum from a ≈ 500 nm thick, 0.3-0.4 at.% Er-doped amorphous layer grown on an oxidized Si wafer at 160°C without an applied bias is shown by

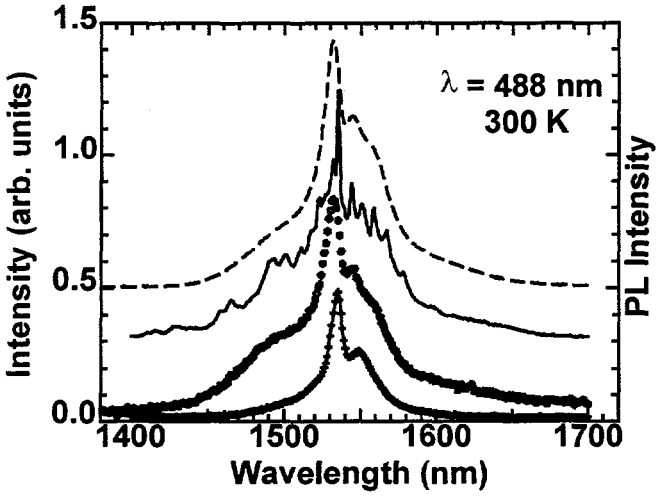

Fig. 3. PL spectra at 300 K from Er in: γ-Al_2O_3 (top), α-Al_2O_3 (solid line), a-Al_2O_3 (open circles), and a-SiO_2 (bottom). Each sample has a layer containing ≈0.2 at.% Er, except a-Al_2O_3 which contains 0.3-0.4 at.% Er.

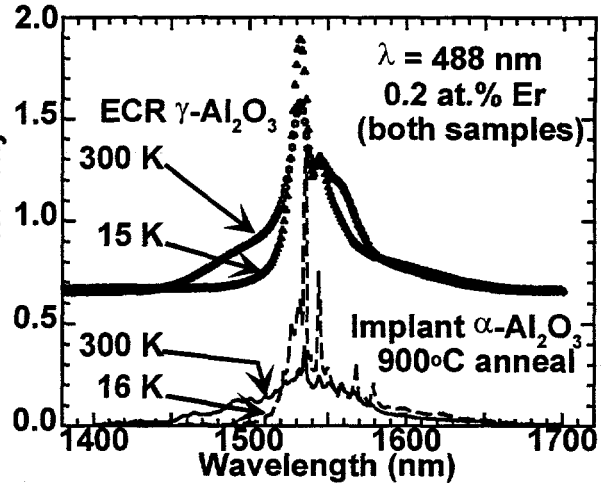

Fig. 4. PL spectra collected at room temperature and cryogenic temperatures from Er in: γ-Al_2O_3 (top curves) and α-Al_2O_3 (bottom curves).

the open circles (τ=0.4 ms).

The influence of local atomic structure on the optical response of the Er dopant can be seen by comparing the peak positions, peak shapes, and PL lifetimes. The curves for the γ-Al_2O_3 and a-Al_2O_3 samples exhibit 3 diffuse shoulders or unresolved peaks around the central peak, similar to the single shoulder for Er in a-SiO_2. These features originate from transitions between the crystal-field split levels of the upper and lower 4f states participating in the de-excitation process. The broadened spectra can indicate significant site-to-site variation in the structural environment seen by the dopant ion, resulting in inhomogeneously broadened peaks. However, the central peak of the a-SiO_2 curve is shifted by 3-4 nm to a higher wavelength than the central peak of the γ-Al_2O_3 and a-Al_2O_3 curves; in fact, the central peak of the α-Al_2O_3 curve is closer to that of the a-SiO_2 curve rather than to the a- or γ-curves. The shift in PL peak position indicates a change in the energies of the participating 4f energy levels and can be directly attributed to a change in the local structural environment of the dopant ion. Contrary to our expectations, the broadened spectra from Er-doped amorphous and large grain γ-Al_2O_3 are similar to each other, and are in contrast to the sharp spectral structure observed from Er in the α-phase host material. Recall that the Er dopant tends to occupy specific structural sites in the hexagonal α-phase matrix: octahedral interstices. The similarity between the amorphous and crystalline γ-phase PL

spectra may be a result of Er occupying both octahedral and tetrahedral sites, randomly, whereas the more distinct features from the sapphire PL spectrum arise from Er occupying primarily the octahedral sites.

The decreased lifetime for the a-Al_2O_3 sample in comparison to the γ-Al_2O_3 sample may be a result of the increased hydrogen content in this sample. A high temperature (>400°C) annealing treatment to release the hydrogen or growth of an amorphous sample with an applied bias is expected to result in a longer τ due to reduced non-radiative de-excitation (see section IV). However, the decreased lifetime for the α phase in comparison to the γ phase, even at cryogenic temperatures, is the result of a different local structural environment for the Er in these two phases. The origin of this difference may lie in slight changes in the electronic environment of the dopant due to local strain or in variations in the nature of the dopant-host atomic bonding.

Figure 4 shows the results of PL measurements at cryogenic temperatures from the γ- and α-phase samples. The relative intensities in this figure can be compared, but note that the curves for the γ-phase sample have been offset by 0.65 for clarity. The PL peaks narrowed at the lower temperatures, as expected for a decrease in the probability for phonon assisted transitions. Further, the peaks below 1520 nm were eliminated at the cryogenic temperatures, for both phases, which suggests that these transitions were phonon assisted at the higher temperature. Also, a broad shoulder at 1560 nm for the γ-phase sample was eliminated at the lower temperature, whereas none of the peaks above 1540 nm from the α-phase sample were eliminated at the lower temperature. Thus, these higher wavelength peaks must be representative of the effect of the sapphire crystal field on the Er^{+3} ion. Also, the central-peak τ for the γ-phase sample increased from 5.7 ms at 300 K to 6.7 ms at 15 K, and τ increased from 2.3 ms at 300 K to 3.3 ms at 16 K for the α-phase sample. Therefore, the cryogenic measurements show even more strongly the differences between the local environment for Er in these two crystalline phases.

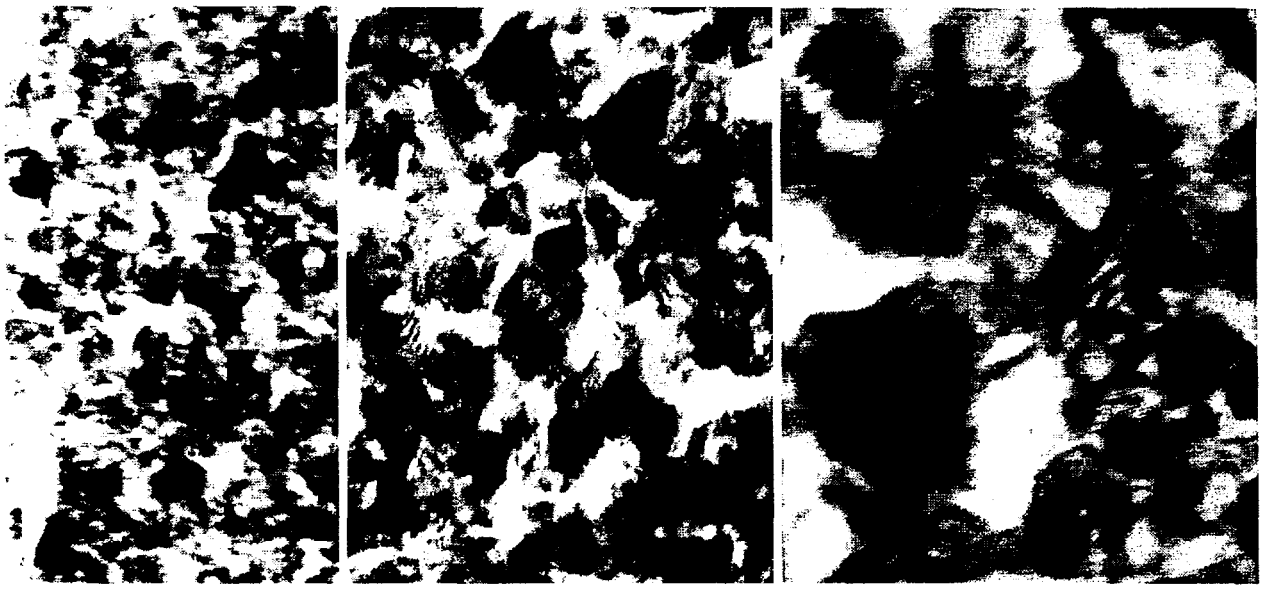

Fig. 5. Bright field TEM images of ECR La_2O_3 deposited at: a) 170°C without an applied bias, b) 170°C with an applied bias of -300 V, and c) 300°C without an applied bias.

In an attempt to keep the lattice structure similar to that found for hexagonal α-Al_2O_3 while changing the effects of phonon coupling, Er-doped La_2O_3 samples were grown at temperatures from 170°C to 300°C and for applied biases from 0 V to 300 V. In contrast to the variation in phase observed with Al_2O_3 deposition from the ECR plasma, the La_2O_3 samples formed only the hexagonal La_2O_3 phase, as shown in Fig. 5 (a=0.4057 nm and c=0.6430 nm). The c-axis lattice constant for hexagonal La_2O_3 is about half that for α-Al_2O_3 and the density of the La_2O_3 phase is only 0.54×10^{23} at/cm^3, about half the atomic density of α-Al_2O_3. The TEM micrographs show that the grain size increases slightly as the bias of the sample is increased at a deposition temperature of 170°C, and the grain size (and distribution of grain sizes) increases further as the temperature is increased without an applied bias.

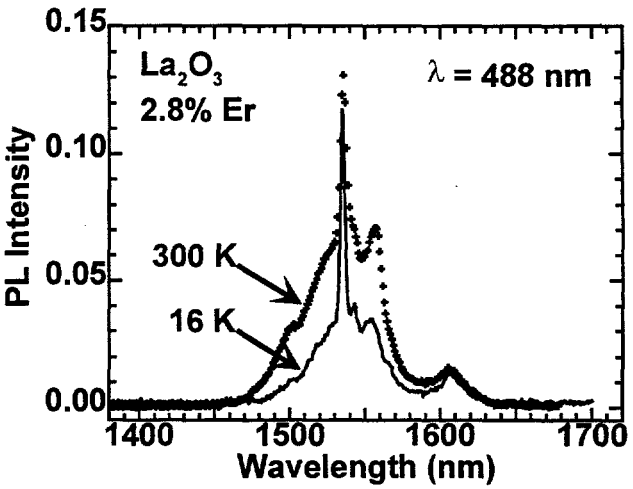

Fig. 6. PL spectra from Er-doped La_2O_3 grown at 300°C without an applied bias.

Although the phase of the lanthanum oxide films remains constant with variation in the deposition temperature and bias, the composition was found to depend strongly on these parameters. This strong compositional dependence was not found for the Al_2O_3 films. For deposition at 170 °C, the hydrogen content in the lanthanum oxide decreased from 20 at.% H to 5 at.% H as the applied bias was increased from 0 V to 300 V. Concurrently, the stoichiometry of the film changed from $La_2O_{4.8}$ to $La_2O_{3.5}$. In both cases, the ratio of extra O (that beyond the stoichiometric composition of La_2O_3) relative to H was approximately 1. This extra amount of O-H can act as absorption centers and decrease the optical quality of the films. A lower H content ($\approx$0.5 at.% H) and stoichiometric La_2O_3 was achieved for a sample grown without an applied bias at 300°C.

The RT and cryogenic PL spectra from an Er-doped La_2O_3 sample grown at 300°C without an applied bias are shown in Fig.6. This sample contains 2.8 at.% Er. The central PL peak wavelength is the same as that for Er in α-Al_2O_3, and the PL peaks found on both sides of this central peak are still present at 16 K, suggesting that phonon-assisted optical transitions have a limited role in this host material relative to that observed for the Al_2O_3 host materials. Also, it is interesting to note that the peak positions, from 1470 nm to 1570 nm, for the La_2O_3 material coincide with the positions for similar peaks in the α-Al_2O_3 material. Therefore, the effect of phonon coupling to Er^{+3} optical transitions can be modified without greatly affecting the crystal-field characteristics of the hexagonal host matrix. One additional intense peak at 1608 nm, however, is observed for luminescence from the Er-doped La_2O_3. The PL lifetime for the central peak at 300 K was 2 ms, similar to that for α-Al_2O_3.

This section showed that the photoluminescence peaks at $\lambda \leq 1520$ nm from Er in an Al_2O_3 matrix are phonon-assisted optical transitions. Also, the PL from Er in amorphous Al_2O_3 is more like that from Er in γ-Al_2O_3 than from Er in sapphire. This result suggests that the local site symmetry for Er in the amorphous phase is similar to that in the γ phase. Further, Er in the γ phase must be randomly distributed near octahedral and tetrahedral sites, whereas Er in α is

predominantly near octahedral sites. The formation of Er-doped, single-crystal γ-Al_2O_3 is needed to precisely determine the lattice site location. Combined use of energetic ions from an ECR plasma and elevated temperatures during growth of Al_2O_3 modified the phase from amorphous to polycrystalline γ, but a single crystal layer has not yet been formed. By changing the host matrix to a heavier mass (La_2O_3), the extent of phonon coupling was decreased.

B. Cluster/Composition Control

More dramatic control of the Er^{+3} local environment was investigated using pulsed laser deposition (PLD) to make novel multiphase nanocomposite materials in which the Er is contained within thin layers which are dispersed in a second, matrix material. These films were fabricated by alternating the ablating laser beam between a target of the majority constituent (either Al_2O_3 or an SiO_2-based glass) and a 1% Er_2O_3-doped $(ZnO)_3(TeO_2)_7$ composite glass (ZTE). For the Al_2O_3-based sample, 50 pairs of Al_2O_3 and ZTE layers were deposited up to a total thickness of 1.4 microns. Each deposited ZTE layer was ~1 nm thick, separated by ~27 nm of Al_2O_3. Photoluminescence (PL) spectra from Er-doped samples were acquired from PLD multiphase, nanocomposite layers and the influence of the local Er environments on the luminescence spectra were compared to the ECR grown and Er-ion implanted single phase alumina.

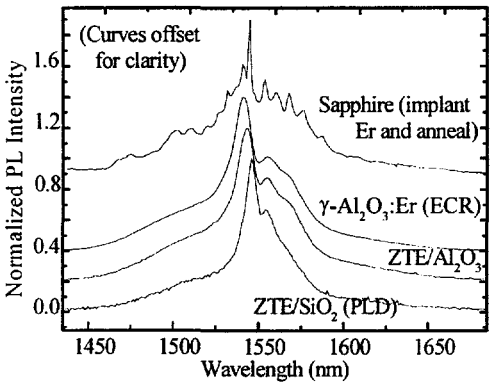

Fig. 7. PL spectra at 300 K from Er in: α-Al_2O_3 (top), γ-Al_2O_3 (second-to-top), ZTE/Al_2O_3 (second-to-bottom), and ZTE/SiO_2 (bottom).

Photoluminescence measurements (488 nm excitation) were performed on samples containing Er^{+3} concentrations of up to 3 atomic percent. Both the influence of local atomic structure and composition on the optical response of the rare-earth dopant can be seen in Fig. 7 for the room temperature PL spectra depicting the $^4I_{13/2}$ to $^4I_{15/2}$ radiative transition in Er^{+3}. The lower three curves all exhibit diffuse shoulders or unresolved peaks around the central peak. These features originate from transitions between the crystal-field split levels of the upper and lower 4f states participating in the de-excitation process. The broadened spectra indicate significant site-to-site variation in the structural environment seen by the dopant ion, resulting in inhomogeneously broadened peaks. This contrasts with the sharp spectral structure observed in an implanted and annealed (900°C) sapphire sample in which the Er dopant tends to occupy specific structural sites in the matrix.

Close examination of these thin film PL results (lower three curves) reveal a significant shift in the central peak wavelength between the single component Er-doped γ-Al_2O_3 and the multiphase, nanocomposite Er-doped ZTE (in both SiO_2 and Al_2O_3). The shift in PL peak position indicates a change in the energies of the participating 4f energy levels and can be directly attributed to a change in the local structural environment of the dopant ion. Moreover, PL lifetime measurements taken from these samples show that the 1.5 micron emission lifetime of Er increases from $\approx$ 2.5 ms in γ-Al_2O_3 to $\approx$ 4.9 ms in ZTE/alumina composites, indicating a

change in the vibrational nature of the local structure and a reduction in nonradiative decay rates. Thus, we have successfully modified the symmetry and vibrational energy of the dopant site and significantly influenced the Er optical behavior.

III. Modeling

A. Ab-Initio Calculations

Initially, the modeling portion of this LDRD was focused on ab-initio calculations of the electronic structure for α-Al_2O_3 using the Sandia computer program QUEST [6]. These results showed that a Density Functional Theory-LDA (local density approximation) treatment reproduces the value of the insulating energy gap (E_{gap}) of sapphire with a discrepancy of only 35% relative to experimental values (see Fig. 8). For comparison, the discrepancies observed for E_{gap} in similar calculations for Si are ~ 50% or more. After geometry and basis set optimization, these calculations produced ground state energies, interatomic distances and electronic densities of states (DOS) in good agreement with experimental and theoretical data. This was important in order to produce a well-controlled referencing system for subsequent calculations of RE-doped Al_2O_3 (see below).

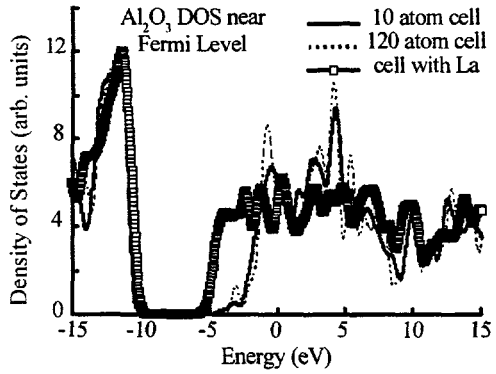

Fig. 8. Calculated density of electronic states for α-Al_2O_3 using two different sized supercells. Also, the effect of adding a lanthanide atom to the structure is shown for comparison.

Two strategies were used to treat a RE impurity substitution on an Al site (to achieve an octahedral coordination). An initial, "minimal" unit cell (10 atom) was used to provide a simple referencing system (amenable to fast calculations) for Al_2O_3 atoms and RE basis function optimizations, and to yield an initial sensible guess of the local lattice expansion around the RE ion. Subsequent calculations utilized a "supercell" model consisting of 120 atom, hexagonal arrangement with La as the central atom. Lanthanum was chosen as a characteristic trivalent rare-earth ion. The latter approach using the 120 atom supercell minimizes size effects in which La atoms in neighboring cells interact. The number of atoms used in the supercell represents the upper computational limit for periodic structures with the present QUEST/Paragon resources. Using the first method, unit cell volume expansion for La substitution on an Al site was found to be 16%. Both total energy/atom and DOS calculations between the small periodic system and the supercell show excellent agreement. Thus, even though translational symmetry arguments were used to reduce the number of k points necessary to perform the energy and DOS calculations in the supercell model, this approach clearly provides a realistic representation of the macroscopic case. The 120-atom cell calculations represent the largest ab initio calculations on an oxide to our knowledge.

In an ideal impurity-like system, no effect should be observable from the presence of neighboring La atoms. Also, little cell-scaling relaxation should be observed (i.e., atoms at the edge of the cell away from the impurity are insensitive to the local modification around the La). The initial runs performed on the La+Al_2O_3 supercell showed that the ideal situation described

above is, to a very good extent, reproduced in the 120 atom cell, where the insertion of La causes a linear cell scaling of only about 0.6%. This is in agreement with the small cell system after proper normalization to the number of atoms. Also, the value of the total energy shows that the chosen scaling value is very close to the optimal (equilibrium) one. Several calculations were performed in order to determine the precise value of the cell scaling and to perform geometry/force optimization. Results indicated a local outward relaxation around the La impurity, whose value is smaller than observed for the 10-atom cell system. In addition, results for the DOS show sensible changes due to the presence of the La ion (e.g., a decrease in E_{gap}).

Table I. Local geometry of Al and substitutional La in α-Al_2O_3

	X-O1 (nm)	X-O2 (nm)	O1-O1 (nm)	O2-O2 (nm)	angle O1-X-O1	angle O1-X-O1	X to O1 plane (nm)	X to O2 plane (nm)
Al_2O_3 (X=Al)	0.185	0.196	0.286	0.251	101.43°	79.36°	0.083	0.132
La:Al_2O_3 (X=La)	0.206	0.247	0.351	0.263	117.10°	64.38°	0.035	0.195

(X stands for either the "octahedral" Al or La in the two structures given: row 1 sapphire; row 2 La-doped sapphire.)

The geometry determined for the relaxed La:Al_2O_3 structure is summarized in Table I row 2, together with bulk Al_2O_3 in row 1. The oxygen atoms are denoted O1 for the lower plane and O2 for the upper plane as shown in Fig. 9. In the relaxed structure, the substitutional La assumes a highly displaced position, moving over 0.05 nm with respect to the original Al site of near octahedral oxygen coordination. The La-O1 distance is significantly smaller than the sum of the ionic radii [7] 0.103 nm (La^{+3}) + 0.138 nm (O^{-2}) = 0.241 nm, and the La-O1 distance is also much smaller than their separation in the La_2O_3 structure (0.246 nm). In comparison, the ab-initio calculations show that the Al-O1 distance agrees well with the experimentally determined distance. Therefore the presence of the RE ion significantly alters the local atomic structure and possibly the local bonding (degree of hybridization).

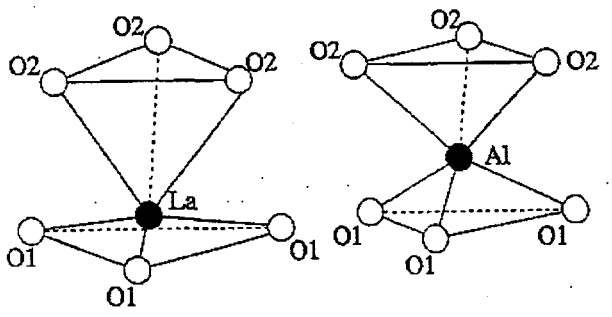

Fig. 9. Calculated equilibrium lattice positions for Al (right) and substitutional La (left) in the octahedral site of the sapphire Al_2O_3 structure.

As shown in Fig. 9, the equilibrium position of the La ion is almost coplanar with the three O1 ions, and its position requires that the La-ion radius is much smaller than the expected ionic radius calculated from La_2O_3. The Madelung potential in La_2O_3 is weaker than in Al_2O_3 because its lattice constants are larger and the atomic density lower. This effect must increase the fractional ionicity (and thus decrease the radius) of substitutional La in alumina vs. La in lanthana, which was indeed born out by charge density calculations from the ab-initio modeling. Higher ionicity reduces the radius at which repulsion balances electrostatic

forces, thus allowing the La to displace toward the O1 plane in response to the electrostatic potential gradient in the alumina. Furthermore, calculation of the partial DOS for La in comparison to the Al shows that La can easily rehybridize its valence electrons, reducing hard-wall repulsion by moving electron density from the 6s-shell into the more compact 5d-orbital, and orient the charge in the 5d-shell to minimize the hard-wall repulsion in a low symmetry site. The energetic cost of rehybridization is recovered by displacing the La toward the O1 plane along the electrostatic potential gradient. These results for La should be of a sufficiently general nature to apply to arguments for fractional ionicity and rehybridization of all the RE ions in alumina, which then predicts displacements toward the O1 plane in a similar fashion. In fact, Alves et al. [4] show experimentally that Er in sapphire displaces toward the O1 plane slightly more than the values computed here for La, which is consistent with the fact that Er is smaller than La. In general then, in systems other than pure compounds, it is clear that simple models for the ionic solids cannot possibly obtain the correct interaction potentials unless fractional ionicity and hybridization are allowed to change.

B. Molecular Dynamic Simulations with Crystal-Field Calculations

In addition to the ab initio calculations using Sandia's massive parallel processing capabilities, we have included molecular dynamic (MD) simulations of Er^{+3} doped γ-Al_2O_3 and α-Al_2O_3 structures through collaborations with researchers at the University of Florida. This is the first time that MD simulations have been used to predict the crystal field splitting of the Er^{+3} energy levels in Al_2O_3. The MD simulations of doped Al_2O_3 yield good estimates of the local environment of Er dopants, and the crystal field splitting from a particular site can be followed over a large number of simulation steps to give information on preferred sites of Er occupation and the effects on the PL spectrum.

Photoluminescence data collected were compared to spectra generated from a molecular dynamics/crystal field analysis of both Er-doped gamma and alpha phase alumina. The MD/CF approach is described in detail elsewhere [8]. In this case, the alumina structure simulation employed a three-body potential function (Blonski and Garfolini [9]) with periodic boundary conditions and a 0.5 fs time step. Gamma and alpha phase structures are formed using 1440 and 810 atoms, respectively, which provides an MD simulation cell containing 27 unit cells in both cases. Erbium was incorporated at randomly distributed octahedral sites in both structures to provide an effective doping level of 6 Er/1440 atoms total and 3 Er/810 atoms total for the gamma and alpha structures, respectively. These doping levels are slightly larger than the range used in the experimental samples (0.3 at%) but provided an increased sampling of possible Er ion local environments. The Er-Al force function parameters were chosen provide consistent agreement with the Er-alumino garnet structure. No interaction between Er atoms was assumed. To generate a reasonable sampling of possible Er local environments, snapshots of the Er-doped alumina structure, previously allowed to equilibrate for 250 ps, were recorded at 10 different time intervals equally spaced between 410000 and 500000 time steps. This procedure was performed for nine and five different starting structures for the gamma and alpha phase alumina simulations, respectively.

Using the collection of Er-local structures produced from the MD simulations, the crystal-field induced energy splitting of the Er 4f manifolds were calculated assuming full ionic

valence charges for the ligands. These calculations utilized Er free-ion crystal field parameters. Contributions from only the electric dipole moment were used to estimate the oscillator strengths for transitions between crystal-field split levels. With the energy positions of the CF-split energy levels within each manifold determined and the corresponding CF-transition oscillator strengths estimated, a simulated emission spectrum of the $^4I_{13/2}$ to $^4I_{15/2}$ transition was generated by assigning a Gaussian lineshape to each possible transition. Convoluting these results over all the Er environments sampled for each simulation enabled a calculated emission spectrum to be developed which was then compared to experiment.

Fig. 10 compares experimental, low temperature PL data with simulated spectra obtained using the MD/CF approach for both gamma and alpha phase hosts. Results from the MD simulations of Er-doped γ-Al_2O_3 showed that the Er local environment exhibited site to site

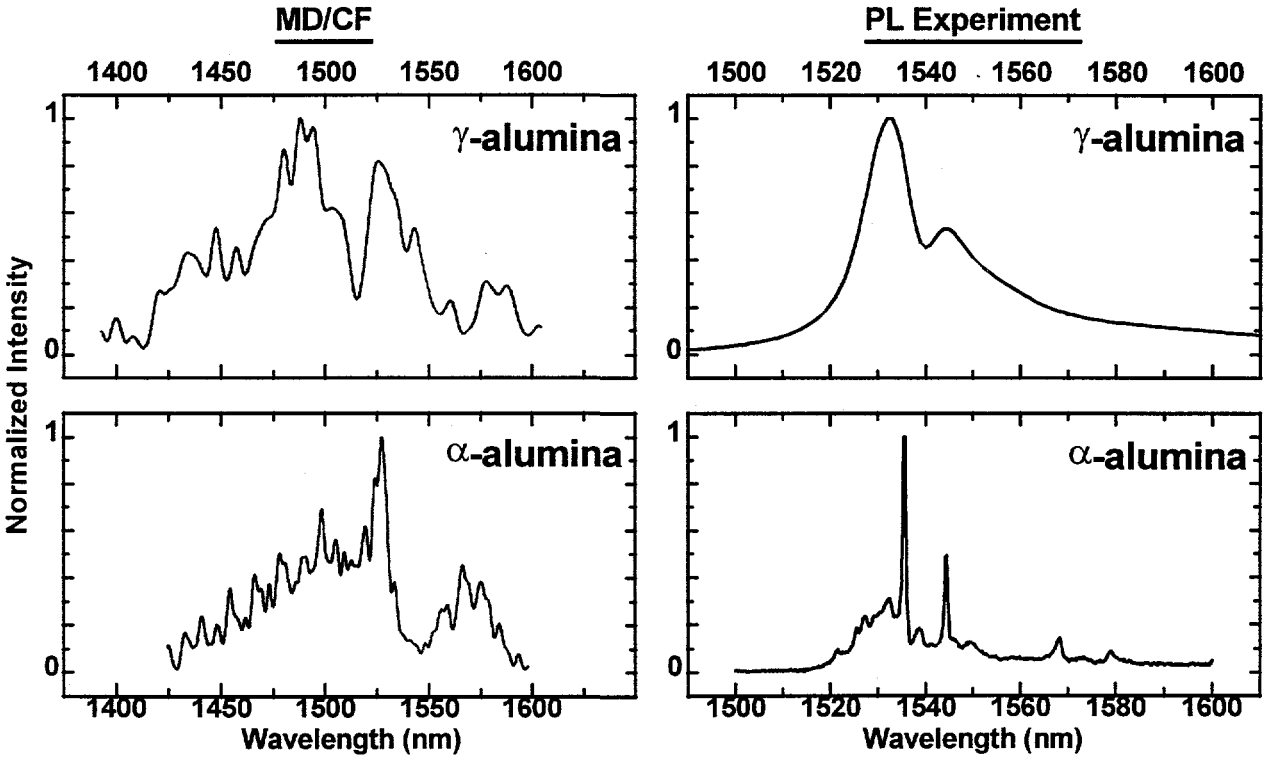

Fig. 10. Simulated photoluminescence spectra (left) from molecular dynamic/crystal-field analyses of Er-doped gamma and alpha alumina are compared to the experimentally measured PL spectra (right) obtained at 15 K from Er-doped gamma and alpha alumina.

variation in symmetry. This is a direct result of the defect spinel structure characterizing the gamma-phase material. Given that only trivalent cations participate in the alumina structure, charge neutrality requires the presence of vacancies on the octa- and tetrahedral sites within the fcc oxygen lattice which would normally be occupied. In this case, only 21.3333 aluminum atoms can exist in the unit cell (compared with a total of 24 di- and trivalent cations in the normal spinel unit cell). As Er is substituted for aluminum into the gamma-alumina structure, its larger size causes a distortion in the immediate environment. This distortion, however, is

mediated by the presence of cation vacancies distributed throughout the structure. This is in contrast to the structural relaxations found for Er in Al substitutional sites in the alpha-phase material. While there is a distortion in the alpha phase structure near the Er substitution, the resulting local symmetry is not influenced by a distribution of neighboring vacancies. In this case, the distortion is reproduced from one Er site to another within the structure, i.e the number of possible distortions generated in the MD simulations is significantly limited compared to gamma-alumina. The Er is found to be displaced from the normal octahedral position of the Al and is located near the closest neighboring oxygen planes as shown above with the ab-initio calculations.

Based on these differences in local site symmetry for Er in the different phases of alumina, distinct differences between the Er emission spectra are anticipated between the alpha and gamma-host phases. In the gamma-phase material, variability in the local site symmetries of the Er environment will produce corresponding differences in the crystal-field splitting energies of the 4f manifolds and, hence, the transition energies between these levels. Such an effect is observed in the CF analysis of the structure, with crystal field splitting energies varying by as much as 20% within the $^4I_{15/2}$ manifold from site to site. In contrast, the relatively limited variability of the Er local site symmetry in the alpha phase material results in well-defined transition energies. Thus, the effects of inhomogeneous broadening in the Er emission spectra are more pronounced in the gamma-phase host material.

This general result is, in fact, observed in the experimental emission data presented in Fig. 10. For comparison, the simulated emission spectra for Er in the two hosts is also provided. While it is clear that the absolute transition energies and oscillator strengths calculated within the crystal field analysis do not agree with experiment, this is not an unexpected result given the assumptions and estimates made in the calculation (e.g. the use of Er free ion wavefunctions and the electric dipole only contribution to the oscillator strength). The width of the Gaussian lineshape used to represent the homogeneous line shape of transitions (in this case, 5 cm-1) between the individual CF-split levels is also an estimate. What is noteworthy about the simulated data is that it predicts the general change in appearance of the Er spectra between the two hosts, i.e. from the sharp structure observed in the alpha-phase alumina to the more broadened line shape characterizing the gamma-phase host. Thus, while the long-range structure of the gamma-phase material (as evidenced by TEM/SAD analyses) indicates a highly crystalline assembly, the unusually broad emission spectrum observed, even at 15K, can be explained in terms of the MD simulation of the Er local environment. In this case, site-to-site variability in the local site symmetry caused by the presence of cation vacancies in the defect spinel structure are shown to produce significant inhomogeneous broadening of the resulting emission lines. Again, the relatively limited range of local symmetries available within the alpha-host significantly limits the site-to-site variability in the transition energies expected, thus resulting in sharper emission structure. Insight into the Er local structural characteristics resulting in the observed emission response of the Er was provided by the MD/CF analysis.

Using a molecular dynamics simulation of the two structures coupled with a crystal field analysis of the Er dopant local environment, these discrepancies between the two experimental spectra can be explained in terms of variability in the local environments. While Er substitution for Al in both crystalline phases promotes local structural distortion, the variability in the nature of this distortion is significantly greater in gamma-alumina owing to the presence of cation vacancies within the structure required to maintain charge neutrality. The variations in the local

site symmetries sampled by the Er population result in correspondingly large changes in the crystal field splitting energies calculated for the 4f manifolds at each Er site and, hence, a greater broadening in the emission bands associated with these levels. Even given the first order assumptions utilized in the CF analysis, this treatment provides insight into the local structural origins of apparently anomalous data.

IV. Controlled Luminescence Efficiency Through Thermal Annealing

Hydrogen in deposited optical ceramics can modify the optical properties, and therefore the role of the hydrogen needs to be understood to control its effects. The previous sections primarily showed that optical performance of Er-doped alumina can be modified through atomic-level engineering of the local structural environment, but the optical performance can also be modified through engineering of the host composition. We have shown above that the shape and lifetime, τ, of the Er PL peak for 1.54 μm emission differs between the alpha, gamma, and amorphous phases of alumina. The PL spectrum for Er in the amorphous phase was nearly identical in shape and peak positions to that for Er in γ-Al_2O_3 and differed from that for Er in α-Al_2O_3. However, τ was different for each of these phases. The difference in local environment may account for the difference in τ between the α and γ phases, but the presence of hydrogen in a-Al_2O_3 was thought to decrease the lifetime for the amorphous phase. Therefore, the one remaining question is to address the effect of H in the amorphous alumina on the luminescence of erbium. This section will examine the thermal release of hydrogen from ECR-deposited alumina and the effect of the hydrogen release on the intensity of the luminescence spectra.

For simplicity in this experiment, visible and near infra-red (IR) light emission from Er-doped a-Al_2O_3 will be stimulated by an ion beam (ionoluminescence) rather then through laser excitation. The samples for this section were made at the floating potential and a deposition temperature of 150-160°C in order to produce the amorphous phase. Erbium-doped amorphous alumina films were deposited using simultaneous electron beam evaporation of aluminum and erbium while bombarding the sample with 30 eV O_2^+ ions from an ECR plasma. The hydrogen content was measured, using elastic recoil detection, as a function of isochronal annealing treatments. The data was fit to a simple trap-release model in order to determine an effective activation energy for the thermal release of H from alumina and Er-doped alumina. The intensity of the ion-beam stimulated luminescence from these samples was monitored in the visible and near infra-red regions at room temperature as a function of the thermal treatments. In order to gain a better understanding of the influence of hydrogen, the ionoluminescence data from samples containing hydrogen were fit with a simple linear equation.

First, the annealing behavior of the a-Al_2O_3 samples with different levels of H content within the matrix were characterized, allowing a determination of the temperature at which the H begins to be released. Then the annealing behavior of Er-doped alumina was characterized and this thermal release behavior was modeled to determine the effective activation energy for thermal release of H, E_{eff}. The hydrogen concentration depth profiles of the Al_2O_3 containing 4 at.% Er are shown in Fig. 11 for the as-deposited film, and after annealing for 30 min. at: 400°C, 500°C, 600°C, and 700°C. It was determined previously that the samples would remain amorphous if annealed below 800°C. The H profile for the sample annealed at 400°C did not differ significantly from the profile for the as-deposited sample. A small amount of hydrogen

was released at 500°C with increasing amounts of hydrogen released for each of the higher annealing temperatures. All of these profiles show a slight gradient increasing with depth, indicating that the H may have a some amount of retrapping during the 30 min. annealing treatment. Retrapping of H will be neglected to first order in the derivation of a simple release model below, but this assumption will be checked by comparing the release energy for two different isochronal annealing times: 30 min. and 4 hr.

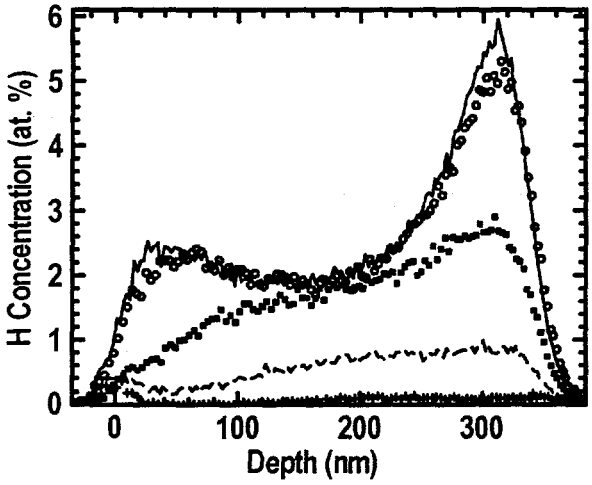

Fig. 11. Hydrogen profiles determined for the as-deposited (solid line) amorphous Al_2O_3 containing 4 at.% Er, and after annealing for 30 min. at: 400°C (O), 500°C (■), 600°C (dashed line), and 700°C (+).

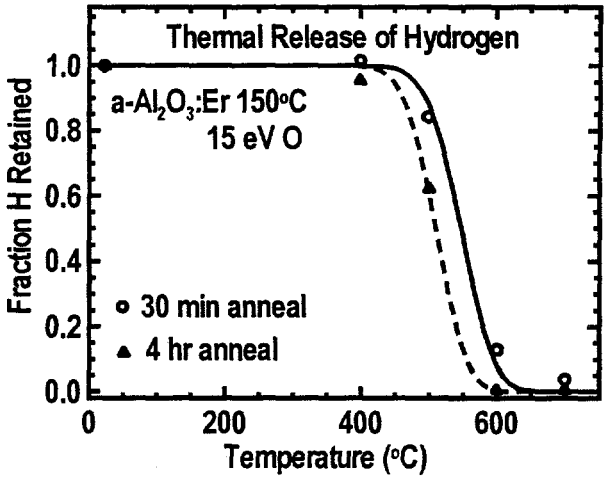

Fig. 12. Fraction of H retained after isochronal annealing treatments. The solid and dashed lines were determined using the model given in the text with $E_{eff} = 2.7$ eV.

Figure 12 shows the experimentally determined fraction of retained hydrogen as a function of annealing temperature for two isochronal annealing times: ● for 30 min. and ▲ for 4 hr. The data are given for the concentration at 1/2 the total depth of the sample and are shown as individual data points. The solid (30 min. anneal) and dashed lines (4hr. anneal) were determined for each of these samples using the initial, as-deposited H concentration and the effective activation energy in the model described below: $E_{eff} = 2.7$ eV. This figure shows that although the 30 min. annealed samples have a H concentration gradient, the energy for release of hydrogen from both of these samples is the same. Therefore the amount of retrapping during the thermal release does not significantly alter the determination of E_{eff}. The same value for thermally activated release of H from undoped alumina was obtained to within 0.05 eV.

Model for Thermally-Activated Release of H. For a single trap energy, the probability (Π) of H thermally escaping a trap at an annealing temperature T is given by an attempt frequency times a Boltzmann factor: $\nu \exp(-E_B/kT)$, where n is the order of 10^{13} s^{-1} for thermal vibrations. After having filled the traps to saturation (assumed to occur during deposition and supported by the fact that annealing below the deposition temperature does not alter the H concentration), the release of H from a trap with energy E_B is governed by a first order rate equation in which the concentration of H in traps at time t is: $d[H]/dt = -\Pi [H]$. The solution to this equation is: $[H(T)] = [H_o(T)] \exp(-\nu\ t \exp(-E_B/kT))$, where $[H_o(T)]$ is the initial H concentration before annealing at temperature T. If a single energy is considered for E_B then the

curves for the thermal release of H as a function of annealing temperature would appear as a step function in which nearly all of the H is released at one temperature. A distribution of trap energies would cause these curves to be rounded. In order to determine how broad is the possible distribution of trap energies, a Gaussian distribution of nine trap energies centered around E_B was used to represent the possible distribution of bonds, angles, and state of relaxation of the amorphous Er-doped Al_2O_3. The standard deviation of the distribution, σ, was minimized to obtain a good fit to the data. The central trap energy will be called E_{eff} because it actually represents a distribution of trap energies, although a narrow distribution, σ=0.1 eV. Thus, the effective activation energy for thermal release of H was determined by fitting the equation above to the data using the measured initial H concentration and t=1800 s (solid line) or 14400 s (dashed line). The E_{eff} determined for both the 30 min. and 4 hr. annealing treatments shown in fig. 2 was 2.7 eV. This activation energy is the same as that determined for undoped a-Al_2O_3 and therefore the effective of even large quantities of Er in the samples of this experiment does not significantly alter the effective release energy for hydrogen.

Both the visible and near IR luminescence spectra were monitored as a function of annealing treatments (hydrogen content). Figure 13 shows the visible region of the IL spectra at 300 K from samples annealed for 4 hr. at 400°C (1.81 at.% H), 500°C (1.35 at.% H), 600°C (0.02 at.% H), and 700°C (0 at.% H). The near infra-red region of the IL spectra are given in Fig. 14. for the samples annealed at 500°C, 600°C, and 700°C. These figures show that the luminescence signal across the entire spectral range increases as the H-content decreases. In fact, a rather dramatic increase in the integrated luminescence is achieved when the samples are annealed such that no measurable H is detected.

The integrated IL signal from the four regions of the visible and near IR regions given in Figs. 13 and 14 are plotted separately in Fig. 15 as a function of hydrogen content in the samples.

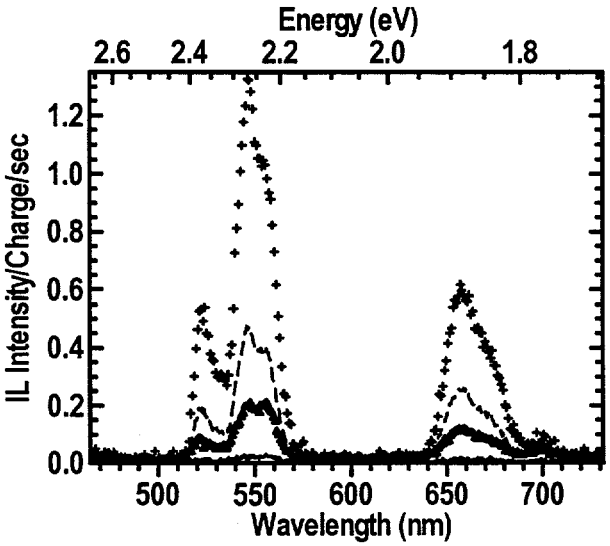

Fig. 13. Visible region of the IL spectra at 300 K from samples annealed for 4 hr. at 400°C (solid line), 500°C (Δ), 600°C (dashed line), and 700°C (+). Respectively, these samples contain: 1.81 at.% H, 1.35 at.% H, 0.02 at.% H, and 0 at.% H.

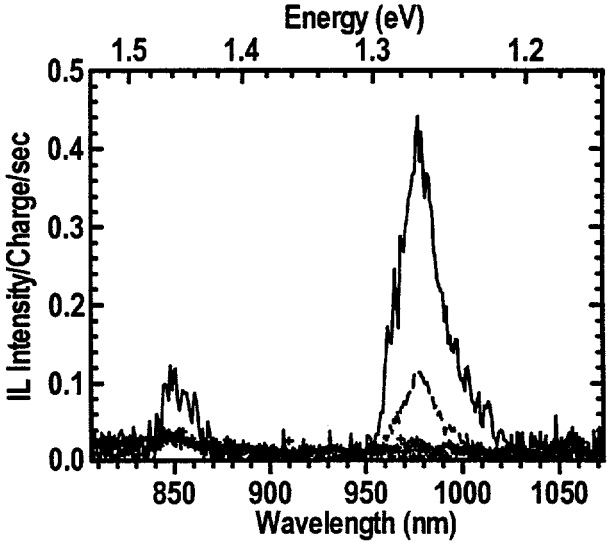

Fig. 14. Near Infra-red region of the IL spectra for the samples annealed at 500°C (+), 600°C (dashed line), and 700°C (solid line). The atomic transitions giving rise to all peaks (Fig.3 & 4) are identified in the text.

As stated above, the luminescence intensity increases with decreasing H content, and once a small amount of H is introduced into the sample the data can be fit by a simple linear equation. A linear fit of data is shown as a heavy solid line: I/I_O = (1-0.72*H/Er)-offset, where I is the integrated IL intensity as a function of H, for the peaks indicated, and I_O is the integrated IL intensity for a sample without any hydrogen. The value of 0.72 is simply the fraction of H which reduces the Er optical activity, and is multiplied by the relative concentration ratio of H/Er. This shows that nearly every H introduced into the sample will eliminate the optical activity of one Er ion. This reduction in optical activity may occur through a direct reduction of the oxidation state of the Er or through other mechanisms which reduce the radiative lifetime of the nearest Er, such as energy transfer to O-H vibrations. Further experimental and theoretical work will be needed to determine the exact cause of the hydrogen effect on luminescence. Finally, it is interesting to note that a rather dramatic reduction in the integrated Il signal occurs for only a small amount of H incorporation as indicated by the offset term in the linear equation. This dramatic decrease is not well understood at this time and so further experimentation with samples containing different amounts of Er with the same H content are needed to help confirm this decrease.

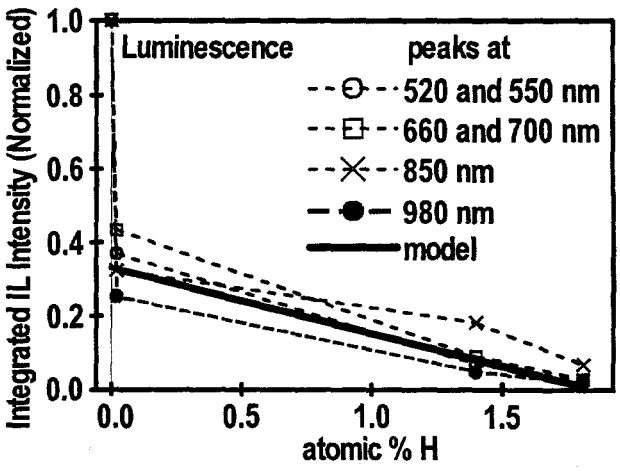

Fig. 15. The integrated IL signal from four regions of the visible and near IR regions are plotted as a function of hydrogen content in the samples (symbols connected by dashed lines). A linear fit of data is shown as a heavy solid line.

V. Conclusions

Optical performance of Er in alumina can be modified by controlling the phase, local composition, and hydrogen content of the host matrix. This work successfully showed that a combination of modeling and experimental verification can be used to understand the primary mechanisms which control the optical performance of rare-earth doped optical ceramic materials.

The method of producing the optical ceramic, including ion irradiation and deposition temperature during growth, modify each of these structural and compositional properties. For example, amorphous alumina is produced at low deposition temperatures and low ion-beam energies while fcc crystalline gamma alumina is produced at high deposition temperatures and high ion-beam energies. It was determined that the local environment for Er or Al in amorphous Al_2O_3 is more like that in γ-Al_2O_3 than sapphire. The Al sites in amorphous alumina are similar to the octahedral and tetrahedral sites surrounded by oxygen in γ-Al_2O_3. The effective activation energies for thermal release of H from amorphous alumina or Er-doped amorphous alumina are the same: $E_{eff} \approx 2.7$ eV.

This paper showed that the photoluminescence peaks at $\lambda \leq 1520$ nm from Er in an Al_2O_3 matrix are phonon-assisted optical transitions. Also, the PL from Er in γ-Al_2O_3 is more like that

from Er in amorphous Al_2O_3 than from Er in sapphire. This result suggests that Er in the γ phase is randomly distributed near octahedral and tetrahedral sites, whereas Er in α is predominantly near octahedral sites. Ab-initio calculations showed that changing fractional ionicity and hybridization are critical to determining the equilibrium position of rare-earth ions in an alumina matrix, and that equilibrium position is displaced away from the Al octahedral position toward the nearest surrounding plane of oxygen atoms. Further, molecular dynamic simulations and crystal-field analysis showed that the discrepancies between the gamma and alpha experimental spectra can be explained in terms of variability in the local Er environments. While Er substitution for Al in both crystalline phases promotes local structural distortion, the variability in the nature of this distortion is significantly greater in gamma-alumina because of the presence of cation vacancies within the structure required to maintain charge neutrality. The variations in the local site symmetries sampled by the Er population result in correspondingly large changes in the crystal field splitting energies calculated for the 4f manifolds at each Er site and, hence, a greater broadening in the emission bands associated with these levels. The formation of Er-doped, single-crystal γ-Al_2O_3 is needed to precisely verify the Er lattice site location in that structure through experimentation.

Combined use of energetic ions from an ECR plasma and elevated temperatures during growth of Al_2O_3 modified the phase from amorphous to polycrystalline γ, but a single crystal layer has not yet been formed. By changing the host matrix to a heavier mass (La_2O_3), the extent of phonon coupling was decreased. The luminescence intensity of the Er-doped alumina samples increases with decreasing H content and the intensity can be fit by a linear relationship in which the optical performance of each Er ion is eliminated by only one hydrogen atom.

VI. References

[1] J.C. Barbour, D.M. Follstaedt, and S.M. Myers, Nucl. Instrum. Methods B **106**, 84 (1995).
[2] P. Villars and L.D. Calvert, Pearson's Handbook of Crystallographic Data for Intermetallic Phases, (American Society for Metals, Metals Park, OH, 1985), pp. 1047-2631.
[3] R.D. Bendale and J.H. Simmons, University of Florida (private communication).
[4] E. Alves, M.F. da Silva, G.N. van den Hoven, A. Polman, A.A. Melo, and J.C. Soares, Nucl. Instrum. Methods B **106**, 429 (1995).
[5] C. Verdozzi, D.R. Jennison, P.A. Schultz, M.P. Sears, J.C. Barbour, and B.G. Potter, Phys. Rev. Lett., accepted (1998).
[6] Written and developed by M. P. Sears and P. A. Schultz at Sandia National Laboratories, Albuquerque, NM 87185-1111.
[7] Periodic Table of the Elements, VCH (1993), compiled by Fluck and Hellman with IUPAC (1991) data.
[8] R.D. Bendale, J.H. Simmons, B.G. Potter, and J.C. Barbour, to be submitted.
[9] S. Blonski and S.H. Garofalini, Surf. Sci. 295, 263 (1993).

Distribution:

1	MS9018	Central Technical Files, 8940-2
2	MS0899	Technical Library, 4916
2	MS0619	Review and Approval Desk, 12690
1	MS0161	Patent and Licensing Office, 11500
1	MS0188	LDRD Office, 4523
1	MS1427	S. T. Picraux, 1100
1	MS1405	C. L. Renschler, 1812
1	MS1056	B. L. Doyle, 1111
1	MS1421	E. B. Stechel, 1153
1	MS1413	T. A. Michalske, 1114
5	MS1056	J. C. Barbour, 1111
5	MS1405	B. G. Potter, 1812
1	MS1056	J. A. Knapp, 1111
1	MS1413	D. R. Jennison, 1114
1	MS1056	D. M. Follstaedt, 1112
1	MS1111	P. A. Schultz, 9225
1	MS1111	M. P. Sears, 9225
1	MS1056	C. H. Seager, 1111
1	MS1405	M. B. Sinclair, 1812